A&A 658, A35 (2022)
https://doi.org/10.1051/0004-6361/202142466

Astronomy & Astrophysics

Host galaxy properties of X-ray active galactic nuclei in the local Universe

L. Koutoulidis[1], G. Mountrichas[2], I. Georgantopoulos[1], E. Pouliasis[1], and M. Plionis[1]

[1] IAASARS, National Observatory of Athens, I. Metaxa & V. Pavlou 1, Penteli 15236, Greece
e-mail: lazkout@noa.gr
[2] Instituto de Fisica de Cantabria (CSIC-Universidad de Cantabria), Avenida de los Castros, 39005 Santander, Spain

Received 17 October 2021 / Accepted 2 November 2021

ABSTRACT

We study the host galaxy properties of active galactic nuclei (AGN) that have been detected in X-rays in the nearby Universe ($z < 0.2$). For that purpose, we use the catalogue provided by the ROSAT-2RXS in the 0.1–2.4 keV energy band, one of the largest X-ray datasets with spectroscopic observations. Our sample consists of ∼900 X-ray AGN. The catalogue provides classification of the sources into type 1 and 2 based on optical spectra. Approximately 25% of the AGN are type 2. We use the available optical, near-IR, and mid-IR photometry to construct spectral energy distributions (SEDs). We measure the stellar mass (M_*) and star formation rate (SFR) of the AGN by fitting these SEDs with the X-CIGALE code. We compare the M_* and SFR of the two AGN populations, taking their different redshift and luminosity distributions into account. Based on our results, type 2 AGN tend to live in more massive galaxies compared to their type 1 counterparts ($\log[M_*(M_\odot)] = 10.49^{+0.16}_{-0.10}$ vs. $10.23^{+0.05}_{-0.08}$), in agreement with previous studies at higher redshifts. In terms of SFRs, our analysis shows that, in the nearby Universe, the number of X-ray AGN that live in quiescent systems is higher compared to at higher redshifts, in accordance with previous studies in the local Universe. However, the majority of AGN (∼75%) live inside or above the main sequence.

Key words. galaxies: nuclei – X-rays: galaxies – methods: data analysis – galaxies: active – methods: observational – galaxies: star formation

1. Introduction

Supermassive black holes (SMBHs), with masses $M_{\rm BH} > 10^6\,M_\odot$, are placed at the centre of most, if not all, galaxies, including our own. Both observations and theoretical models have shown that there is a linear relation between the growth of a SMBH and the host galaxy evolution (Magorrian 1998; Ferrarese & Merritt 2000; Gebhardt 2000; Häring & Rix 2004; Kormendy & Ho 2013). However, the details of the physical mechanism that connects them are still not well understood.

The growth of the SMBH occurs when matter falls into the inner region of the galaxy in the proximity of the SMBH. As it grows, the SMBH releases huge amounts of energy across the entire electromagnetic spectrum. In such cases, the inactive galaxy turns into an active galactic nucleus (AGN; e.g., Hickox & Alexander 2018, and references therein).

X-rays are one of the most reliable methods of detecting AGN; this is because a large part of the AGN population, the obscured sub-sample, is detected in X-rays but not in the optical regime of the spectrum (Hasinger 2008; Hickox & Alexander 2018, and references therein). Obscured AGN represent a considerable fraction of the total AGN population (e.g., Akylas et al. 2006; Ueda et al. 2014). Therefore, studying the origin and nature of obscured AGN in order to reveal the complete AGN population constitutes a significant challenge. Some studies claim that different levels of obscuration correspond to different stages of SMBH growth (evolutionary model; e.g., Ciotti & Ostriker 1997; Hopkins et al. 2006, 2008; Somerville et al. 2008). Those observations contradict geometric models such as the unification model, in which the observed differences between type 1 and type 2 properties depend on the viewing angle at which the AGN is observed (Antonucci 1993; Urry & Padovani 1995; Netzer 2015).

One approach to examining whether type 1 and 2 AGN constitute the same or different populations is to examine the properties of their host galaxies. There are two main parameters that are related to the early stages of the formation and evolution of galaxies, namely their stellar mass and star formation rate (SFR; Kauffmann et al. 2003). Previous studies have used different criteria to classify AGN (e.g., X-ray criteria based on the hardness ratio or the hydrogen column density, optical spectra, or optical-mid-IR colours).

Mountrichas et al. (2021b) and Masoura et al. (2021) analysed X-ray AGN observed by the Chandra X-ray Observatory within the 9.3 deg^2 Boötes field of the NOAO Deep Wide-Field Survey (NDWFS) and X-ray AGN in XXL-North, respectively. They concluded that X-ray absorption is not linked with the properties of the galaxy. Lanzuisi et al. (2017) used X-ray AGN in the COSMOS field and found that, although, obscured and unobscured AGN have similar SFRs, unobscured AGN tend to have lower stellar masses than their obscured counterparts. Suh et al. (2019) examined the effects of the nuclear activity on the star formation in both type 1 and type 2 AGN host galaxies in the COSMOS field and found that it is not conclusive whether AGN activity plays a role in quenching the star formation in galaxies. They proposed that stellar mass might be the primary factor related to the suppression of both star formation and AGN activity.

Recent studies that used optical criteria to classify their sources found that both populations have similar SFRs but that type 2 AGN tend to reside in more massive galaxies than their type 1 counterparts (e.g., Zou et al. 2019; Mountrichas et al. 2021b). Shimizu et al. (2015) used 122 ultra-hard X-ray AGN at $z < 0.05$ from the *Swift* Burst Alert Telescope (BAT; Barthelmy et al. 2005) and found similar SFRs for the two AGN

types, but their results suggest that, in the local Universe, a high fraction of both type 1 and 2 AGN live in quiescent systems.

In the present work we utilise a large, spectroscopic X-ray sample provided by the SPIDERS-2RXS survey to examine the host galaxy properties of type 1 and 2 AGN. Their classification is based on optical spectra. This catalogue provides the largest systematic spectroscopic observations of an X-ray-selected sample to date, making it an ideal laboratory for studying AGN and their host galaxies. We construct the spectral energy distribution (SEDs) of the sources using optical, near-IR, and mid-IR photometry and use the X-CIGALE code to fit these SEDs. Our goal is to examine the host galaxy properties of the two AGN types and compare our findings with AGN at higher redshifts (e.g., Zou et al. 2019; Mountrichas et al. 2021b) and in the local Universe (e.g., Shimizu et al. 2015) that have also been classified via optical criteria.

2. Data

In this study we use the DR16-SPIDERS-2RXS catalogue. The catalogue is fully described in Comparat et al. (2020). In brief, this dataset utilises the second ROSAT all sky survey source catalogue (hereafter 2RXS), which contains approximately 135 000 X-ray detections in the 0.1−2.4 keV energy band, with a likelihood threshold of 6.5 (Boller et al. 2016). A novel Bayesian statistics-based algorithm, NWAY (Salvato et al. 2018), was used to find reliable counterparts at other wavelengths. Then, the SDSS spectroscopic information was added based on the optical position in the SPIDERS-DR16 footprint (Dwelly et al. 2017). This resulted in 19821 X-ray sources, 10336 of which are AGN, that cover an area of 5128 deg^2 with a flux limit of $f_x = 10^{-12.5}$ erg s^{-1} cm^{-2}. In addition to the optical (SDSS) photometry, sources also have near-IR photometry from 2MASS (Skrutskie et al. 2006) and mid-IR photometry from allWISE (Wright et al. 2010) datasets.

Following Comparat et al. (2020), we selected objects with reliable redshifts (CONFBEST==3), excluding 'STARS', 'GALAXIES' and 'QSO' that belong to a cluster of galaxies. According to Boller et al. (2016), a detection likelihood threshold >6.5 leads to a large fraction of spurious sources (∼30%). Thus, we adopted a stricter threshold for the detection criterion, specifically exiML > 10. To focus on the nearby Universe, we selected sources with spectroscopic redshifts $z < 0.2$. We also restricted our sample to those AGN with X-ray luminosity, $L_X > 10^{42}$ erg s^{-1}, to avoid contamination by non-AGN systems. After applying the above criteria, our sample consisted of 1021 sources.

To classify sources as unobscured-type 1 AGN (broad emission lines) and obscured-type 2 AGN (narrow emission lines), we used the spectral classification provided in Comparat et al. (2020). We considered as type 1 sources with spectroscopic classes '*BLAGN*', '*QSO*', '*BALQSO*', and '*QSO − BAL*'. As type 2 AGN we included sources with the spectroscopic class '*NLAGN*'. Our sample consists of 760 type 1 and 255 type 2 AGN at $z < 0.2$.

3. Analysis

In this section we describe the SED fitting process we performed to estimate the galaxy properties (SFR and stellar mass) and present the requirements we applied to include only sources with the most robust measurements in our analysis.

3.1. X-CIGALE

To calculate the properties of the galaxies that host the X-ray AGN of the sample used in this work, we performed SED fitting. For that purpose, we used the X-CIGALE code (Yang et al. 2020), which is a new branch of the CIGALE fitting algorithm (Boquien et al. 2019) and has been used widely in the literature (e.g., Pouliasis et al. 2020). X-CIGALE can model the X-ray emission of galaxies and the presence of polar dust that accounts for extinction of the UV and optical emission in the poles of AGN (Yang et al. 2020; Mountrichas et al. 2021b). In our analysis, we did not use the X-ray flux, f_X, of the AGN in the fitting process. X-CIGALE requires the intrinsic (i.e. the X-ray-absorption-corrected) X-ray flux of the source. The X-ray absorption is known for ∼73% of our sources (Boller et al. 2016). Thus, including the f_X in our SED fitting process would reduce the size of our sample without affecting the stellar mass or SFR measurements (Mountrichas et al. 2021b). Alternatively, observed but hard (e.g., 2–10 keV) X-ray fluxes can be included in the fitting analysis (Yang et al. 2020) since at these energies the X-ray flux is only mildly affected by the X-ray absorption. However, these energy bands are not available for our dataset.

A delayed star formation history model, with the functional form SFR $\propto t \times \exp(-t/\tau)$, was applied to build the galaxy component. The model also includes a star formation burst in the form of constant ongoing star formation that is not allowed to be longer than 50 Myr. Stellar emission was modelled using the Bruzual & Charlot (2003) single stellar populations template with a Salpeter initial mass function and metallicity equal to the solar value (0.02). Stellar emission was attenuated following Charlot & Fall (2000). The IR SED of the dust heated by stars was implemented with the Dale et al. (2014) model, without the AGN component. Active galactic nucleus emission was modelled using the SKIRTOR templates (Stalevski et al. 2012, 2016). SKIRTOR is a clumpy two-phase torus model that considers an anisotropic, but constant, disk emission. A detailed description of the SKIRTOR implementation in (X-)CIGALE is given in Yang et al. (2020). The AGN fraction, frac$_{\rm AGN}$, is defined as the ratio of the AGN IR emission to the total IR emission of the galaxy. A polar dust component (E_{B-V}) was added and modelled as a dust screen absorption and a grey-body emission. The Small Magellanic Cloud (SMC) extinction curve (Prevot et al. 1984) was adopted. Re-emitted grey-body dust was parameterised with a temperature of 100 K and an emissivity index of 1.6. The modules and input parameters we used in our analysis are presented in Table 1.

In our analysis we did not fix the inclination angle to a value that corresponds to the optical classification of the AGN. The addition of polar dust in the fitting process makes the definition of obscured and unobscured AGN more complex. The UV-optical SED of type 2 AGN is not affected, since it is already absorbed by the dusty torus. However, polar dust reddens the UV-optical SED of type 1 AGN. A detailed discussion on the effect of polar dust on the AGN classification by X-CIGALE and its comparison with the optical classification is provided in Sect. 5.1 of Mountrichas et al. (2021b). Their analysis also shows that the misclassification of some sources by X-CIGALE does not affect the reliability of the host galaxy measurements. The modules and input parameters we used in our analysis are presented in Table 1.

3.2. Exclusion of sources with unreliable measurements

It is important in our analysis to only keep sources for which the SFR and stellar mass estimates are reliable. To this end, we first excluded sources whose fit had reduced χ^2, $\chi^2_{\rm red} > 5$. This criterion is based on visual inspection of the SED fits and has been adopted in previous studies (e.g., Masoura et al. 2018;

Table 1. Models and the values for their free parameters used by X-CIGALE for the SED fitting of our galaxy sample.

Parameter	Model/values
Star formation history: delayed model and recent burst	
Age of the main population	1000, 5000, 7000, 9000, 10 000, 11 000, 12 000 Myr
e-folding time	1000, 3000, 5000, 7000, 9000, 10 000, 11 000, 12 000 Myr
Age of the burst	50 Myr
Burst stellar mass fraction	0.0, 0.005, 0.01, 0.015, 0.02, 0.05, 0.10, 0.15, 0.18, 0.20
Simple stellar population: Bruzual & Charlot (2003)	
Initial mass function	Salpeter
Metallicity	0.02 (Solar)
Galactic dust extinction	
Dust attenuation law	Calzetti et al. (2000)
Reddening $E(B-V)$	0.0, 0.1, 0.2, 0.3, 0.4, 0.5, 0.6, 0.7, 0.8, 0.9
Galactic dust emission: Dale et al. (2014)	
α slope in $\mathrm{d}M_{\mathrm{dust}} \propto U^{-\alpha} dU$	1.0, 1.5, 2.0, 2.5, 3.0
AGN module: SKIRTOR)	
Torus optical depth at 9.7 microns $\tau_{9.7}$	3.0, 7.0
Torus density radial parameter p ($\rho \propto r^{-p} e^{-q\lvert\cos(\theta)\rvert}$)	1.0
Torus density angular parameter q ($\rho \propto r^{-p} e^{-q\lvert\cos(\theta)\rvert}$)	1.0
Angle between the equatorial plan and edge of the torus	40°
Ratio of the maximum to minimum radii of the torus	20
Viewing angle	30° (type 1), 70° (type 2)
AGN fraction	0.0, 0.01, 0.1, 0.2, 0.3, 0.4, 0.5, 0.6, 0.7, 0.8, 0.9, 0.99
Extinction law of polar dust	SMC
$E(B-V)$ of polar dust	0.0, 0.2, 0.4
Temperature of polar dust (K)	100
Emissivity of polar dust	1.6

Notes. For the definitions of the various parameters, see Sect. 3.1.

Table 2. Number of X-ray AGN used in the different parts of our analysis (see text for more details).

	Stellar mass	SFR	$\mathrm{SFR_{norm}}$
Total AGN	944	860	859
Type 1	729	673	672
Type 2	215	187	187

Mountrichas et al. 2019; Buat et al. 2021). Increasing the limit to $\chi^2_{\mathrm{red}} > 6$ adds more sources to our sample, but most of them have bad fits and thus unreliable host galaxy measurements. Reducing the threshold to $\chi^2_{\mathrm{red}} > 4$ would exclude additional sources, the vast majority of which have reliable fits. This criterion eliminates 133 AGN (9% of the sample). For each parameter calculated by the SED fitting process, X-CIGALE estimates two values. One is evaluated from the best-fit model, and one weights all models allowed by the parametric grid, with the best-fit model having the heaviest weight (Boquien et al. 2019). This weight is based on the likelihood, $\exp(-\chi^2/2)$, associated with each model. A large difference between these two values for a specific parameter indicates that the fitting process did not result in a reliable estimation for this parameter (Mountrichas et al. 2021a,c; Buat et al. 2021). Thus, when we compared the stellar masses of type 1 and 2 AGN, we only included in our analysis sources with $\frac{1}{5} \leq \frac{M_{*,\mathrm{best}}}{M_{*,\mathrm{bayes}}} \leq 5$, where $M_{*,\mathrm{best}}$ and $M_{*,\mathrm{bayes}}$ are the best-fit and Bayesian-fit values of M_*, respectively. This method to exclude unreliable estimations has been applied in recent studies (Mountrichas et al. 2021a,c; Buat et al. 2021). Using different values for the boundaries of the criterion (i.e. 0.1–0.33 for the lower limit and 3–10 for the upper limit) does not affect the results of our analysis. This criterion reduces the sample to 944 X-ray AGN (93% of the initial dataset). Of these systems, 729 are type 1 and 215 are type 2 (Table 2). Similarly, for the comparison of the SFR of the two AGN types, we require $\frac{1}{5} \leq \frac{\mathrm{SFR_{best}}}{\mathrm{SFR_{bayes}}} \leq 5$, where $\mathrm{SFR_{best}}$ and $\mathrm{SFR_{bayes}}$ are the best and Bayesian values of the SFR, respectively, estimated by X-CIGALE. This reduces our sample to 860 X-ray AGN (85% of the initial dataset). Of these sources, 673 are type 1 and 187 are type 2. We note that throughout our analysis we used the Bayes calculations of X-CIGALE for the various parameters.

In Fig. 1 we present examples of SEDs from the sources used in our analysis. The top panels show AGN classified as type 1 based on their optical spectra. The bottom panels present AGN with an optical classification of type 2. Figure 2 presents the stacked SEDs at rest frame for the AGN type 1 and type 2 samples. The median SEDs of the total emission (host galaxy and AGN components) are plotted with solid lines, while the shaded areas correspond to the 15th up to the 85th percentiles at each wavelength. The lower panel shows the ratio of the host dust and stellar attenuated emission of the two populations. This plot is further discussed in Sect. 4.

3.3. Reliability of SFR measurements

The SFRs were calculated using the emission of young stars that emit most of their light in the UV (e.g., Schreiber et al. 2015). Most of this light is absorbed by interstellar dust and is then re-emitted in the IR part of the spectrum. Mountrichas et al. (2021b,c) showed, using X-ray samples from the Boötes and XMM-XXL fields, that the absence of far-IR photometry

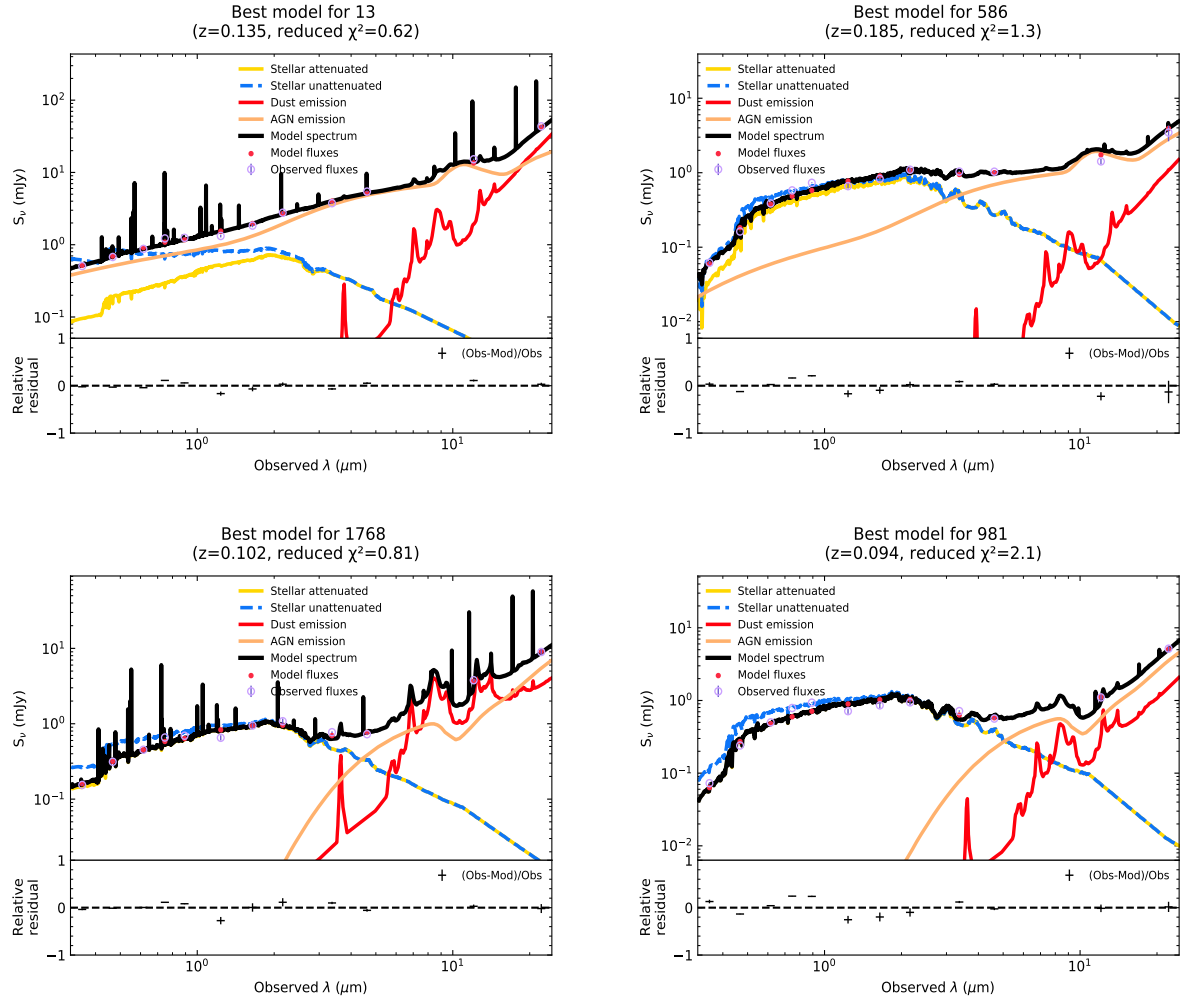

Fig. 1. Examples of SEDs from sources used in our analysis. The *top panels* present AGN classified as type 1 based on their optical spectra. Their SFR and stellar mass are $\log[\mathrm{SFR}(M_\odot\,\mathrm{yr}^{-1})] = 1.63$, $\log[M_*(M_\odot)] = 10.06$ (*top, left panel*) and $\log[\mathrm{SFR}(M_\odot\,\mathrm{yr}^{-1})] = -0.45$ and $\log[M_*(M_\odot)] = 10.75$ (*top-right panel*), respectively. The *bottom panel* presents the SEDs of two AGN classified as type 2 based on their optical spectra. Their SFR and stellar mass are $\log[\mathrm{SFR}(M_\odot\,\mathrm{yr}^{-1})] = 1.87$, $\log[M_*(M_\odot)] = 10.30$ (*bottom, left panel*) and $\log[\mathrm{SFR}(M_\odot\,\mathrm{yr}^{-1})] = -1.0$ and $\log[M_*(M_\odot)] = 10.24$ (*bottom-right panel*), respectively.

(*Herschel*) does not affect the SFR measurements. At high redshifts ($z > 0.5$), the *u* optical band is redshifted to rest-frame wavelengths of <2000 Å, where radiation from young stars is emitted. However, at lower redshifts shorter wavelengths are required.

To examine whether the absence of UV photometry affects our SFR measurements, we cross matched our X-ray sample with the GALEX dataset. There are 114 X-ray AGN that have UV counterparts within a radius of 1″. For these sources, we performed SED analysis with and without the far-UV and near-UV bands of GALEX, using in both cases the same parameter space in the fitting process. Figure 3 presents the comparison of the SFR measurements for the 89 sources that have $\chi^2_{\mathrm{red}} < 5$ in both runs. Although the sample is small, our results indicate that the two measurements are consistent. The scatter appears larger at SFR<0, but there is no systematic offset between the two calculations. The mean absolute difference of the SFR estimates is 0.25 dex for type 1 AGN (blue circles) and 0.31 dex for type 2 AGN (red circles).

4. Results

In this section we compare the SFR and stellar mass of the two AGN types. For the calculation of these two host galaxy properties, we applied SED fitting using the grid described in Sect. 3.1. Figures 4 and 5 present the redshift and bolometric luminosity, L_{bol}, distributions of the two AGN populations. Bolometric luminosities were calculated using the AGN, stellar, and dust luminosities that were measured via the SED fitting process. To compare the host galaxy properties of the two subsamples, we first accounted for their different redshift and luminosity distributions. To this end, we assigned a weight to each source using the procedure described as follows. The redshift distributions of the two AGN types were joined and normalised to the total number of sources in each redshift bin (in bins of 0.1). We repeated the same process for the luminosity distributions (in bins of 0.1 dex). This effectively gives us the probability density function (PDF) of each source in this 2D (L, z) parameter space. Then, each source was weighted based on its luminosity and redshift, $w_{L,z}$, according to the estimated PDF (e.g., Mountrichas et al. 2019, 2021b,c). We also used an additional weight that accounts for the uncertainties of the stellar mass and SFR calculations. Specifically, we calculated the significance (*sigma* = value/uncertainty) of each stellar mass, $sigma_{M_*}$, and SFR, $sigma_{\mathrm{SFR}}$, measurement and weighted each source based on these values, in addition to the weight that accounts for the redshift and luminosity of each source (Masoura et al. 2021).

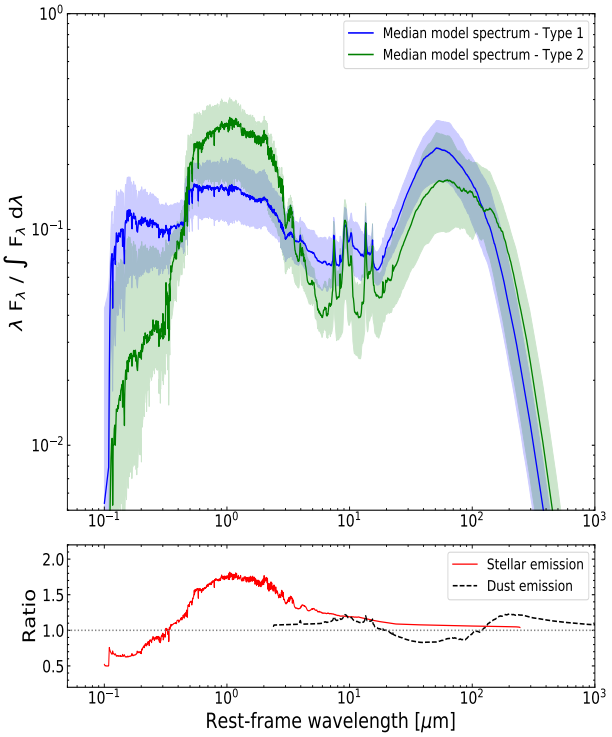

Fig. 2. Stacked SEDs at rest frame for the type 1 (blue) and type 2 (green) AGN samples. The median SEDs of the total emission (host galaxy and AGN components) are plotted with solid lines, and the shaded areas correspond to the 15th up to the 85th percentiles at each wavelength. The *lower panel* shows the ratio of the host dust and stellar attenuated emission of the two populations.

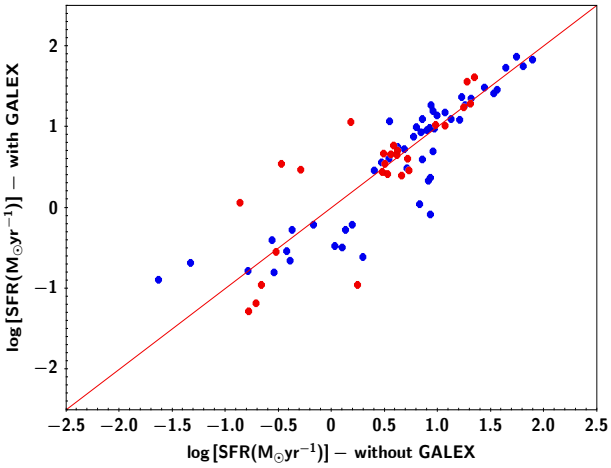

Fig. 3. Comparison of SFR measurements with and without GALEX photometry for the 89 X-ray AGN that have available far-UV and near-UV and $\chi^2_{\rm red} < 5$ in both runs. The solid line marks the 1:1 relation. Results show that there is no systematic offset between the two measurements. The mean absolute difference of the SFR estimates is 0.25 dex for type 1 AGN (blue circles) and 0.31 dex for type 2 AGN (red circles).

Thus, the total weight, w_t, assigned to each source is given by the equation

$$w_t = w_{L,z} \times sigma_{M_*} \times sigma_{\rm SFR}. \quad (1)$$

Figure 6 presents the stellar mass distributions of type 1 and 2 X-ray AGN for the 944 sources that meet our selection criteria (Sect. 3.2). We notice that the M_* of type 2 sources (red

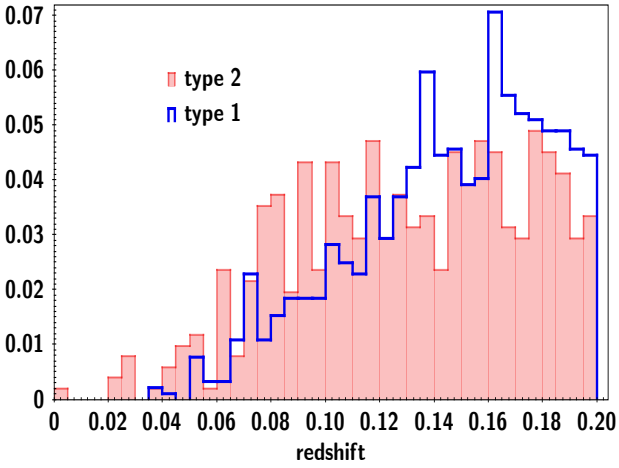

Fig. 4. Redshift distributions of type 1 (blue histogram) and type 2 (red histogram) AGN.

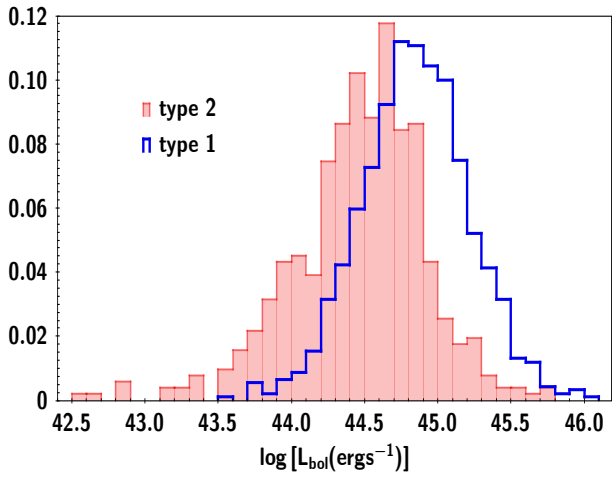

Fig. 5. Distributions of bolometric luminosity, $L_{\rm bol}$, of type 1 (blue histogram) and type 2 (red histogram) AGN. The $L_{\rm bol}$ has been calculated using the AGN, stellar, and dust luminosities as measured by the SED fitting process.

histogram) is shifted to slightly higher values compared to that of type 1 AGN (blue line histogram). The median stellar mass of type 1 AGN is $\log[M_*(M_\odot)] = 10.23^{+0.05}_{-0.08}$, while that of type 2 is $10.49^{+0.16}_{-0.10}\,M_\odot$. Errors were calculated using bootstrap resampling (e.g., Loh 2008). The stacked SEDs presented in Fig. 2 also reveal that type 2 AGN (green line) have higher stellar mass than their type 1 counterparts (blue line). Although the result is marginally significant ($\sim 2\sigma$), it is in agreement with similar studies at higher redshifts. Mountrichas et al. (2021c) used X-ray AGN in the XMM-XXL field at $0.1 < z < 0.9$ and found that type 2 AGN tend to live in host galaxies with stellar masses that are higher by ~0.3 dex compared to their type 1 counterparts. Their classification is based on optical spectra (Menzel et al. 2016). Zou et al. (2019) classified AGN in the COSMOS field using optical spectra, morphology, and optical variability. They found that type 2 AGN prefer to reside in more massive galaxies than type 1 at all the redshifts included in their sample (see their Fig. 6).

In Fig. 7 we present the SFR distributions of type 1 and 2 X-ray AGN for the 860 sources that meet our selection criteria (Sect. 3.2). We notice that the distributions of both AGN

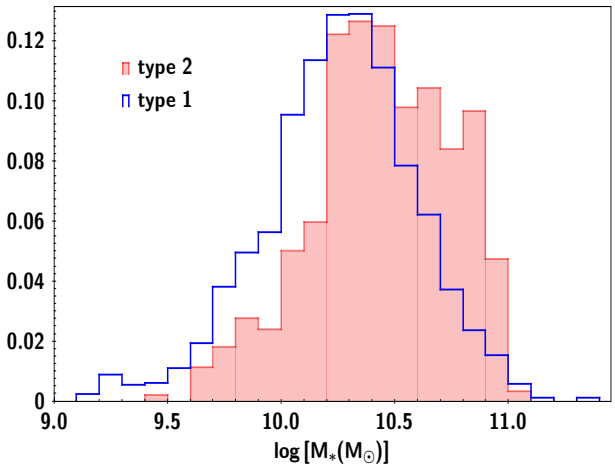

Fig. 6. Stellar mass distributions of type 1 (blue line histogram) and type 2 (red shaded histogram) X-ray AGN. Type 2 sources tend to reside in more massive systems compared to their type 1 counterparts. The median stellar mass of type 1 AGN is $\log[M_*(M_\odot)] = 10.23^{+0.05}_{-0.08}$, while that of type 2 is $10.49^{+0.16}_{-0.10}\,M_\odot$. Errors have been calculated using bootstrap re-sampling.

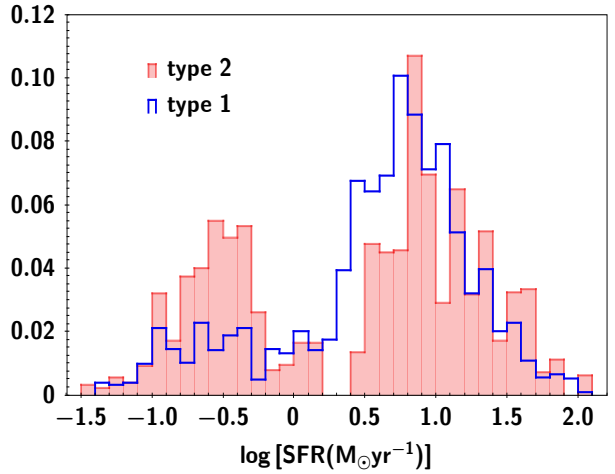

Fig. 7. SFR distributions of type 1 (blue line histogram) and type 2 (red histogram) AGN. Distributions of both AGN populations peak at similar SFR values, $\log[\mathrm{SFR}(M_\odot\,\mathrm{yr}^{-1})] \sim 0.7{-}0.8$. However, type 2 AGN present a second, lower peak at $\log[\mathrm{SFR}(M_\odot\,\mathrm{yr}^{-1})] \sim -0.5$. The SFR distribution of type 1 AGN also has a tail that extends to low SFR values, but this tail is not as prominent as in the case of type 2 AGN.

populations peak at similar SFR values, $\log[\mathrm{SFR}(M_\odot\,\mathrm{yr}^{-1})] \sim 0.7{-}0.8$. However, type 2 AGN present a second, lower peak at $\log[\mathrm{SFR}(M_\odot\,\mathrm{yr}^{-1})] \sim -0.5$. The SFR distribution of type 1 AGN also has a tail that extends to low SFR values, but this tail is not as prominent as in the case of type 2 AGN. Figure 2 shows that, overall, type 1 AGN have higher star formation than the type 2 population, which can be attributed to the large tail that the SFR distribution of type 2 AGN presents at low values. Similar studies at higher redshifts (Zou et al. 2019; Mountrichas et al. 2021c) find that both AGN types have similar SFR distributions and that these distributions do not extend to low SFR values. However, Shimizu et al. (2015) used ultra-hard X-ray-selected AGN from the *Swift* BAT at $z < 0.05$. They found that a large fraction of their type 1 and 2 AGN lies below the main sequence (MS).

To examine the position of the AGN relative to the MS in our sample, we estimated the $\mathrm{SFR_{norm}}$ parameter. The $\mathrm{SFR_{norm}}$ is defined as the ratio of the SFR of AGN to the SFR of star-forming MS galaxies with the same stellar mass and redshift (e.g., Masoura et al. 2018, 2021; Bernhard et al. 2019). For the SFR calculation of MS galaxies, we used expression 9 from Schreiber et al. (2015). In this part of the analysis, we required both the SFR and stellar mass criteria mentioned in Sect. 3.2 to be fulfilled. These requirements were met by 859 AGN. The $\mathrm{SFR_{norm}}$ distributions of type 1 and 2 AGN are shown in Fig. 8. The vertical dashed line indicates the position of the MS. Based on our results, there is a large fraction of AGN, in particular type 2 AGN, that live in quiescent systems. In Table 3 we present the fraction of type 1 and 2 AGN that live inside, below, and above the MS. Following a similar approach to that of Shimizu et al. (2015), we considered an AGN to be inside the MS when its $\mathrm{SFR_{norm}}$ value is within $0 \pm 1\,\sigma$, where $1\sigma = 0.3$ dex. The AGN with $\mathrm{SFR_{norm}} > 0.3$ live in star-forming galaxies, while AGN with $\mathrm{SFR_{norm}} < -0.3$ reside in quiescent systems. Our results show that about half of type 2 AGN live in quiescent systems. This is in agreement with the results of Shimizu et al. (2015) (see their Table 1). However, Shimizu et al. find a similar fraction of quiescent systems for type 1 AGN. In our case, the fraction of type 1 AGN that are below the MS is significantly lower compared to type 2. We note, however, that the host galaxy properties were estimated following different approaches in the two studies. In Shimizu et al., the SFR was estimated using IR luminosities, and stellar mass measurements are based on the $g - i$ colour (see their Sects. 3 and 4 for more details). Furthermore, Shimizu et al. (2015) define their own MS, using galaxy

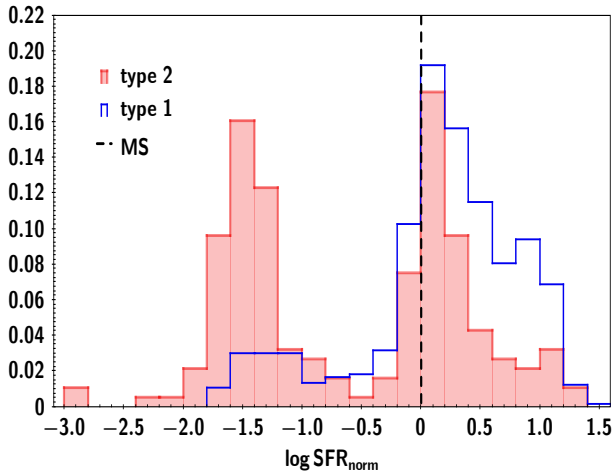

Fig. 8. Distributions of the $\mathrm{SFR_{norm}}$ of type 1 (blue line) and type 2 (red shaded histogram) AGN. Our results show that, in the local Universe ($z < 0.2$), there is a significant fraction of X-ray AGN that live in quiescent systems ($\mathrm{SFR_{norm}} < 0$). This appears to be more prominent in the case of type 2 AGN.

Table 3. Numbers and fractions of type 1 and 2 AGN that live inside, below, and above the MS.

	Above MS	Inside MS	Below MS
672 type 1	305 (45%)	260 (39%)	107 (16%)
187 type 2	30 (16%)	62 (33%)	95 (51%)

Notes. We consider an AGN to be inside the MS when its $\mathrm{SFR_{norm}}$ value is within $0 \pm 1\,\sigma$, where $1\sigma = 0.3$ dex. AGN with $\mathrm{SFR_{norm}} > 0.3$ live in star-forming galaxies, while AGN with $\mathrm{SFR_{norm}} < -0.3$ reside in quiescent systems.

samples for which they estimate the SFR and M_*, by applying similar methods as for their AGN sample. In this work we used a relation from the literature to estimate the SFR of MS galaxies (Schreiber et al. 2015). This approach hints at a number of systematics (Mountrichas et al. 2021c). For these reasons, a strict comparison between the two studies cannot be made.

In total, 202 of the AGN in our dataset (24%), 107 type 1 and 95 type 2, live in quiescent systems. Compared to similar studies at higher redshifts, this fraction appears high. Mountrichas et al. (2021a) found that ∼12% of the AGN population has $\mathrm{SFR_{norm}} < -0.3$ (∼8% of type 1 and ∼14% of type 2; see their Fig. 6). However, the fraction of quiescent host galaxies found in our study is lower than that found in the local Universe (z<0.05; Shimizu et al. 2015). It is well known that the fraction of quiescent systems in the overall (non-AGN) galaxy population increases with cosmic time, in particular for the more massive sources (e.g., Fontana et al. 2009). About 10% of galaxies are quiescent at $z \sim 3-4$. The fraction goes up to ∼50% at $z \sim 1.5$ and increases even further in the local Universe (e.g., Domínguez Sánchez et al. 2011; Pandya et al. 2017). As previously mentioned, the definition of quiescent galaxies is not strict and our approach to defining such systems hints at systematics; nevertheless, our analysis shows that the fraction of sources that host AGN and are quiescent does not appear to be higher than the fraction of quiescent systems in the overall galaxy population. Thus, our results do not seem to support a picture in which AGN suppress the SFR of their host galaxy. Overall, we conclude that our results corroborate that, in the local Universe, the fraction of X-ray AGN that live in quiescent systems is higher than that at higher redshifts. This may be more evident in the case of type 2 AGN. However, the majority of AGN live inside or above the star-forming MS.

5. Summary

We have used data from the DR16-SPIDERS-2RXS catalogue to examine the host galaxy properties of type 1 and 2 X-ray AGN at $z < 0.2$. The classification is based on optical spectra. We used optical, near-IR, and mid-IR photometry to construct the SEDs of the sources, and we fitted these SEDs using the CIGALE code. After applying various selection criteria to exclude sources with unreliable stellar mass and SFR measurements, we ended up with ∼900 X-ray sources.

We took the different redshift and luminosity distributions of the two AGN types into account and compared their stellar masses and SFRs. We also accounted for the uncertainties of the measurements of the two galaxy properties, which were calculated by CIGALE.

Our analysis shows that type 2 AGN reside in more massive galaxies compared to their type 1 counterparts. Based on our results, type 1 AGN live in galaxies with stellar mass $\log[M_*(M_\odot)] = 10.23^{+0.05}_{-0.08}$, while type 2 reside in galaxies with $10.49^{+0.16}_{-0.10}\,M_\odot$. This finding is in accordance with similar studies at higher redshifts (Zou et al. 2019; Mountrichas et al. 2021b).

To investigate the position of X-ray AGN relative to the MS, we calculated the $\mathrm{SFR_{norm}}$ parameter. Previous studies (Shimizu et al. 2015) found a large fraction of AGN living in quiescent galaxies at $z < 0.05$. Our results corroborate that in the local Universe there is an increased number of AGN (24%) that live in quiescent systems compared to at higher redshifts. However, the majority of AGN live either inside or above the star-forming MS.

Acknowledgements. Lazaros Koutoulidis (L.K.) acknowledges support from the State Scholarship Foundation (IKY). G. M. acknowledges support by the Agencia Estatal de Investigación, Unidad de Excelencia María de Maeztu, ref. MDM-2017-0765. I. G. and E. P. acknowledge financial support by the European Union's Horizon 2020 programme "XMM2ATHENA" under grant agreement No 101004168. The research leading to these results has received funding from the European Union's Horizon 2020 programme under the AHEAD2020 project (grant agreement n. 871158).

References

Akylas, A., Georgantopoulos, I., Georgakakis, A., Kitsionas, S., & Hatziminaoglou, E. 2006, A&A, 459, 693
Antonucci, R. 1993, ARA&A, 31, 473
Barthelmy, S. D., Barbier, L. M., Cummings, J. R., et al. 2005, Space Sci. Rev., 120, 143
Bernhard, E., Grimmett, L. P., Mullaney, J. R., et al. 2019, MNRAS, 483, L52
Boller, T., Freyberg, M. J., Trümper, J., et al. 2016, A&A, 588, A103
Boquien, M., Burgarella, D., Roehlly, Y., et al. 2019, A&A, 622, A103
Bruzual, G., & Charlot, S. 2003, MNRAS, 344, 1000
Buat, V., Mountrichas, G., Yang, G., et al. 2021, A&A, 654, A93
Calzetti, D., Armus, L., Bohlin, R. C., et al. 2000, ApJ, 533, 682
Charlot, S., & Fall, S. M. 2000, ApJ, 539, 718
Ciotti, L., & Ostriker, J. P. 1997, ApJ, 487, L105
Comparat, J., Merloni, A., Dwelly, T., et al. 2020, A&A, 636, A97
Dale, D. A., Helou, G., Magdis, G. E., et al. 2014, ApJ, 784, 83
Domínguez Sánchez, H., Pozzi, F., Gruppioni, C., et al. 2011, MNRAS, 417, 900
Dwelly, T., Salvato, M., Merloni, A., et al. 2017, MNRAS, 469, 1065
Ferrarese, L., & Merritt, D. 2000, ApJ, 539, 9
Fontana, A., Santini, P., Grazian, A., et al. 2009, A&A, 501, 15
Gebhardt, K., et al. 2000, ApJ, 543, 5
Häring, N., & Rix, H.-W. 2004, ApJ, 604, L89
Hasinger, G. 2008, A&A, 490, 905
Hickox, R. C., & Alexander, D. M. 2018, ARA&A, 56, 625
Hopkins, P. F., Hernquist, L., Cox, T. J., et al. 2006, ApJS, 163, 1
Hopkins, P. F., Hernquist, L., Cox, T. J., & Keres, D. 2008, ApJS, 175, 356
Kauffmann, G., Heckman, T. M., White, S. D. M., et al. 2003, MNRAS, 341, 54
Kormendy, J., & Ho, L. C. 2013, ARA&A, 51, 511
Lanzuisi, G., Delvecchio, I., Berta, S., et al. 2017, A&A, 602, A123
Loh, J. M. 2008, ApJ, 681, 726
Magorrian, J., et al. 1998, AJ, 115, 2285
Masoura, V. A., Mountrichas, G., Georgantopoulos, I., et al. 2018, A&A, 618, A31
Masoura, V. A., Mountrichas, G., Georgantopoulos, I., & Plionis, M. 2021, A&A, 646, A167
Menzel, M.-L., Merloni, A., Georgakakis, A., et al. 2016, MNRAS, 457, 110
Mountrichas, G., Georgakakis, A., & Georgantopoulos, I. 2019, MNRAS, 483, 1374
Mountrichas, G., Buat, V., Yang, G., et al. 2021a, A&A, 646, A29
Mountrichas, G., Buat, V., Georgantopoulos, I., et al. 2021b, A&A, 653, A70
Mountrichas, G., Buat, V., Yang, G., et al. 2021c, A&A, 653, A74
Netzer, H. 2015, ARA&A, 53, 365
Pandya, V., Brennan, R., Somerville, R. S., et al. 2017, MNRAS, 472, 2054
Pouliasis, E., Mountrichas, G., Georgantopoulos, I., et al. 2020, MNRAS, 495, 1853
Prevot, M., Lequeux, J., Maurice, E., Prevot, L., & Rocca-Volmerange, B. 1984, A&A, 132, 389
Salvato, M., Buchner, J., Budavári, T., et al. 2018, MNRAS, 473, 4937
Schreiber, C., Pannella, M., Elbaz, D., et al. 2015, A&A, 575, A74
Shimizu, T. T., Mushotzky, R. F., Meléndez, M., Koss, M., & Rosario, D. J. 2015, MNRAS, 452, 1841
Skrutskie, M. F., Cutri, R. M., Stiening, R., et al. 2006, AJ, 131, 1163
Somerville, R. S., Hopkins, P. F., Cox, J. T., Robertson, B. E., & Hernquist, L. 2008, MNRAS, 391, 481
Stalevski, M., Fritz, J., Baes, M., Nakos, T., & Popović, L. Č. 2012, MNRAS, 420, 2756
Stalevski, M., Ricci, C., Ueda, Y., et al. 2016, MNRAS, 458, 2288
Suh, H., Civano, F., Hasinger, G., et al. 2019, ApJ, 872, 168
Ueda, Y., Akiyama, M., Hasinger, G., Miyaji, T., & Watson, M. G. 2014, ApJ, 786, 104
Urry, C. M., & Padovani, P. 1995, PASP, 107, 803
Wright, E. L., Eisenhardt, P. R. M., Mainzer, A. K., et al. 2010, AJ, 140, 1868
Yang, G., Boquien, M., Buat, V., et al. 2020, MNRAS, 491, 740
Zou, F., Yang, G., Brandt, W. N., & Xue, Y. 2019, ApJ, 878, 11